Journal of Ceramic Processing Research. Vol. 21, No. 4, pp. 416~424 (2020)
(Received 28 December 2019, Received in revised form 21 April 2020, Accepted 4 May 2020)
https://doi.org/10.36410/jcpr.2020.21.4.416

J O U R N A L O F
Ceramic Processing Research

Preparation and characterization of hexaferrites $Ba_{0.40}Sr_{0.60-x}Nd_xFe_{12.00-x}Zn_xO_{19}$ by the solid-state reaction route

Yujie Yang*, Xiansong Liu, Shuangjiu Feng, Xucai Kan, Qingrong Lv, Feng Hu, Jiangli Ni, Chaocheng Liu and Wei Wang

Engineering Technology Research Center of Magnetic Materials, School of Physics & Materials Science, Anhui University, Hefei 230601, P. R. China

The microstructural, spectral, magnetic and electric properties of hexaferrites $Ba_{0.40}Sr_{0.60-x}Nd_xFe_{12.00-x}Zn_xO_{19}$ ($0.00 \le x \le 0.30$) synthesized by the solid-state reaction route have been studied. XRD results confirmed that the hexaferrites with Nd-Zn content (x) of $0.00 \le x \le 0.24$ were single M-type phase, and the hexaferrite with x = 0.30 exhibited the M-type phase and impurity phase. The remanence (B_r) increased with x from 0.00 to 0.06, and then decreased when $x \ge 0.06$. The intrinsic coercivity (H_{cj}) and magnetic induction coercivity (H_{cb}) decreased with x from 0.00 to 0.30. B_r indicated a linear decreasing behavior with increasing temperature from 20 °C to 140 °C. H_{cj} raised linearly with increasing temperature from 20 °C to 140 °C. The value of a_{Br} basically remained constant with Nd-Zn content (x). The value of a_{Hcj} increased with x from 0.00 to 0.12, and began to decrease when $x \ge 0.12$. The electrical resitivity (ρ) presented a decreasing trend with x from 0.00 to 0.30.

Key words: M-type hexaferrites, Solid-state reaction route, X-ray diffraction, Magnetic measurements.

Introduction

Hexagonal ferrites have received considerable attention of researchers and engineers since the discovery of the ferrite in the 1950s. Although not as powerful as the newest NdFeB or $SmCo_5$ magnets, they still have a large market share in the market of magnetic materials, because of their perfect chemical stability, high Curie temperature, high performance-price ratio, and easy methods of production [1, 2]. In addition, M-type hexaferrites can be widely utilized as microwave devices, permanent magnetic materials, radar communication and microwave devices [3-5]. Many preparation techniques have been used to prepare the M-type hexaferrites such as hydrothermal method [6], three-step calcination method [7], co-precipitation method [8], standard solid-state reaction route [9], molten flux calcination method [10], sol-gel method [11], pulsed laser deposition method [12], and extrusion-based three-dimensional (3D) printing [13]. In the above-mentioned methods, the solid-state reaction route was used to fabricate the hexaferrites because of a few several profitable factors, for example controllable grain size, low manufacturing cost, simple technology and high productive.

In order to modify the intrinsic magnetic properties of M-type hexaferrites, the M-type hexaferrites been doped with rare-earth metals and transition metals, or the combination of these [14-36]. Singh et al. reported the rare-earth substitution (La^{3+}, Nd^{3+} and Sm^{3+}) doped strontium ferrite (Sr-M), and the results exhibited that the magnetization moment (M_s) and remenance (M_r) decrease with increasing rare-earth ions substitution, while the enhancement of H_c values may be due to higher magnetocrystalline anisotropy [15]. The Nd-substituted strontium hexaferrites prepared by hydrothermal synthesis have been reported by Wang et al. [17], and it is found that Nd substitution with a Nd-Sr ratio of 1/8 enhances the coercivity without causing any significant deterioration in either the saturation magnetization or the remanence. Shekhawat et al. synthesized the La-Sm substituted Sr-hexaferrite $SrAl_4(La_{0.5}Sm_{0.5})_xFe_{8-x}O_{19}$ ($0.0 \le x \le 1.5$) nanomaterials by the auto combustion method and found that the remanence magnetization increases while intrinsic coercivity decreases with substitution [18]. The Zn-doped Ba hexaferrite single crystals have been synthesized, and it is found that Zn substitution significantly influences the coercivity and magnetization of Ba hexaferrite while the Curie temperature was nearly constant over the range of doping [23]. Zhang et al. reported the Nd-Co doped strontium hexaferrites $Sr_{1-x}Nd_xFe_{12-x}Co_xO_{19}$ ($0.0 \le x \le 0.4$) fabricated by sol-gel autocombustion method, and the results showed that Nd-Co substitution can improve the saturation magnetization and coercivity and reaches a maximum at x=0.2 [33]. Liu et al. prepared the Ce-Zn co-substituted M-type strontium hexaferrites by the ceramic method, and the results showed that M_s and H_c can be improved significantly [36].

*Corresponding author:
Tel : +86 551 63861257
Fax: +86 831 63861257
E-mail: loyalty-yyj@163.com

In this article, in order to enhance the magnetic properties, we have selected a combination of Nd^{3+} and Zn^{2+} ions to substitute in the M-type Ba-Sr hexaferrites. The hexaferrites $Ba_{0.40}Sr_{0.60-x}Nd_xFe_{12.00-x}Zn_xO_{19}$ ($0.00 \leq x \leq 0.30$) were successfully synthesized by the solid-state reaction route. Impact of Nd-Zn co-doping on the microstructural, spectral and electric properties was analyzed. Subsequently, the magnetic properties of hexaferrites with different Nd-Zn content (x) were systematically investigated under different temperatures from room temperature (20 ºC) to 140 ºC. The novelty of this work is doing a study on the temperature coefficient of remanence (B_r) (a_{Br}), and temperature coefficient of intrinsic coercivity (H_{cj}) (a_{Hcj}) for the Nd-Zn co-doped hexaferrites.

Experimental Details

The hexaferrites $Ba_{0.40}Sr_{0.60-x}Nd_xFe_{12.00-x}Zn_xO_{19}$ ($0.00 \leq x \leq 0.30$) were prepared via the solid-state reaction route [37]. Barium carbonate ($BaCO_3$), strontium carbonate ($SrCO_3$), metallic oxides (Nd_2O_3, Fe_2O_3 and ZnO) were weighted in stoichimetric ratio. And then, the raw materials were thoroughly mixed together in water for 10 h in a ball mill in order to obtain finely mixed powder. Further, the as-mixed powder was dried, and pressed into circular pellets with Φ30 × 16 mm. Subsequently, the pellets were calcined in a muffle furnace at 1,260 ºC for 2.0 h. The calcined pellets were shattered in a vibration mill, and suitable additives ($CaCO_3$ 0.8 wt%, SiO_2 0.2 wt% and Al_2O_3 0.2 wt%) were added, then the mixture was wet-milled in a ball-mill for 16 h. This procedure guarantees a narrow particle size distribution with the mean size of around 0.75 μm. The fine milled hexaferrite slurry was pressed into circular pellets with Φ30 × 16 mm in a magnetic field of 1.2 T. In order to measure the DC electrical resitivity, the fine milled hexaferrite slurry was dried, and then pressed into circular pellets with Φ20 × 8 mm. Finally, all green pellets were sintered in a muffle furnace at 1,185 ºC for 1.5 h.

The phase identification and structural characterization of synthesized samples were performed by X-ray diffraction (XRD, Rigaku Smartlab). The surface morphology of the hexaferrites was detected by a field emission scanning electron microscopy (FE-SEM, HITACHI S-4800). The magnetic properties were measured at different temperatures from room temperature (20 ºC) to 140 ºC using a Hysteresis graph meter (NIM-2000HF, National Institute of Metrology of China). (Resistivity testing system, Ningbo rooko FT-353) was used to measure the DC electrical resitivity (ρ) of the hexaferrites at room temperature.

Results and Discussion

Fig. 1 presents the XRD patterns of hexaferrites

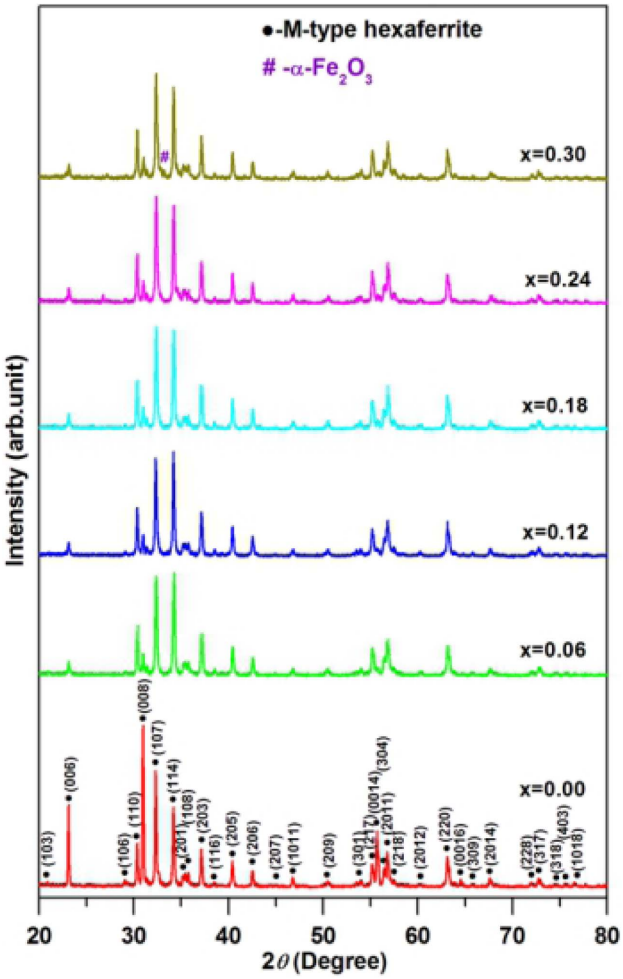

Fig. 1. XRD patterns of the hexaferrites $Ba_{0.40}Sr_{0.60-x}Nd_xFe_{12.00-x}Zn_xO_{19}$ with different Nd-Zn content (x).

$Ba_{0.40}Sr_{0.60-x}Nd_xFe_{12.00-x}Zn_xO_{19}$ with different Nd-Zn content (x). The characteristics peaks were compared with the M-type hexaferrite ICCD card No. 51-1879. It can be observed that the hexaferrites $Ba_{0.40}Sr_{0.60-x}Nd_xFe_{12.00-x}Zn_xO_{19}$ with Nd-Zn content (x) ≤ 0.24 belonged to M-type hexagonal crystal structure. The presence of hematite (α-Fe_2O_3) (ICCD card no. 89-0599) detected for the hexaferrite with Nd-Zn content (x) = 0.30 might be due the incomplete reaction under the preparing conditions. These show that the maximum doped content of Nd-Zn co-doping can not exceed x = 0.24.

The lattice parameters *c* and *a* of the hexaferrites $Ba_{0.40}Sr_{0.60-x}Nd_xFe_{12.00-x}Zn_xO_{19}$ were calculated using to the following formula [38].

$$d_{hkl} = \left(\frac{4}{3} \cdot \frac{h^2 + hk + k^2}{a^2} + \frac{l^2}{c^2} \right)^{-1/2} \quad (1)$$

In the given relation, d_{hkl} is the interplaner spacing of the lines in XRD pattern and *h*, *k* and *l* are the Miller indices. The values of lattice parameters *c* and *a* for the hexaferrites $Ba_{0.40}Sr_{0.60-x}Nd_xFe_{12.00-x}Zn_xO_{19}$ with different Nd-Zn content (x) are listed in Table 1. The values of *c*

Table 1. The values of molecular weight, lattice parameters (*c* and *a*), unit cell volume (V_{cell}), X-ray density (d_{xrd}), and bulk density (d_{bulk}) for the hexaferrites $Ba_{0.40}Sr_{0.60-x}Nd_xFe_{12.00-x}Zn_xO_{19}$ with different Nd-Zn content (x).

Nd-Zn content (x)	Molecular weight	*c* (Å)	*a* (Å)	V_{cell} (Å^3)	d_{xrd} (g/cm^3)
0.00	1081.69	23.1057	5.8802	691.9	5.194
0.06	1085.66	23.0926	5.8791	691.2	5.218
0.12	1089.63	23.0828	5.8780	690.7	5.241
0.18	1093.59	23.0644	5.8769	689.9	5.266
0.24	1097.56	23.0455	5.8760	689.1	5.292
0.30	1101.53	23.0189	5.8734	687.7	5.321

and *a* decrease with increasing Nd-Zn content (x) from 0.00 to 0.30. The possible explanation for the decrease of *c* and *a* with increasing Nd-Zn content (x) can be attributed to the difference in the ionic radii (Δr) of the metal ions and the number of ionic substitutions of each species. Substitution of Sr^{2+} (r = 1.180 Å) by Nd^{3+} (r = 0.983 Å) makes a negative difference in the ionic radii of Δr = -0.197 Å. Substitution of Fe^{3+} (r = 0.645 Å) by Zn^{2+} (r = 0. 740 Å) makes a positive difference in the ionic radii of Δr = +0.095 Å. As in the case of Nd-Zn content (x) = 0.12, the lattice parameter *c* and *a* are decreased.

The unit cell volume (V_{cell}) of the hexaferrites $Ba_{0.40}Sr_{0.60-x}Nd_xFe_{12.00-x}Zn_xO_{19}$ was calculated from the following equation [38]:

$$V_{cell} = \frac{\sqrt{3}}{2} a^2 c \tag{2}$$

And its values are summarized in Table 1. It is clearly seen that the unit cell volume (V_{cell}) decreases with Nd-Zn content (x) from 0.00 to 0.30. The decrease in the V_{cell} is due to the decrease of lattice parameters *c* and *a* with increasing Nd-Zn content (x) as shown in Table 1. The X-ray density (d_{xrd}) has been calculated by using the below formula [39]:

$$d_{xrd} = \frac{ZM}{N_A V_{cell}}, \tag{3}$$

where *Z* is the number of molecular per unit cell, *M* is the molecular weight, N_A is Avogadro's number and V_{cell} is unit cell volume. And the values d_{xrd} are listed in Table 1. It noticed that the value of $d_{X\text{-}ray}$ enhances from 5.194 g/cm^3 at x = 0.00 to 5.321 g/cm^3 at x = 0.30. The enhancement of d_{xrd} with increasing Nd-Zn content (x) can be attributed to the larger molecular weight and decreasing trend of unit cell volume (V_{cell}) for the Nd-Zn co-doped hexaferrites displayed in Table 1.

Fig. 2 shows the FE-SEM images of the hexaferrites $Ba_{0.40}Sr_{0.60-x}Nd_xFe_{12.00-x}Zn_xO_{19}$ with x = 0.00, x = 0.12, and x = 0.24. This indicates that the grains in the hexaferrites are homogeneous distribution with hexagonal plate like shape. The average grain size increases from 1.8 μm at x = 0.00 to 3.2 μm at x = 0.24.

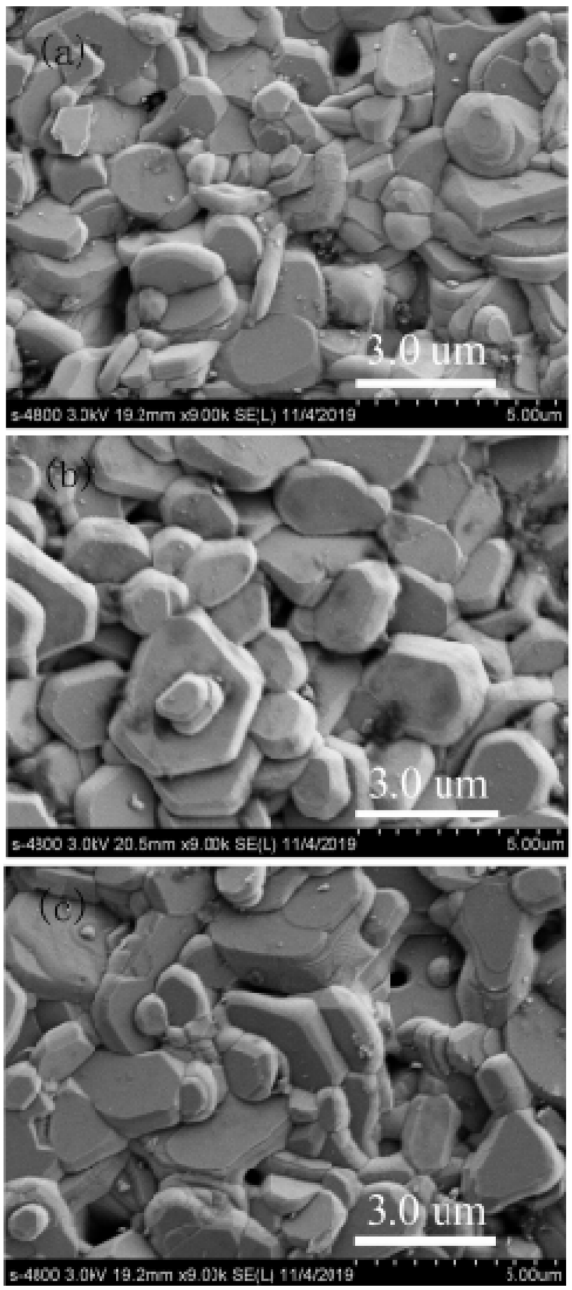

Fig. 2. FE-SEM images of the hexaferrites $Ba_{0.40}Sr_{0.60-x}Nd_xFe_{12.00-x}Zn_xO_{19}$ with (a) x=0.00, (b) x=0.12, and (c) x=0.24.

Fig. 3 represents the room temperature demagnetizing curves of the hexaferrites $Ba_{0.40}Sr_{0.60-x}Nd_xFe_{12.00-x}Zn_xO_{19}$ with different Nd-Zn content (x). As revealed by the demagnetizing curves, the magnetic properties of the hexaferrites are greatly influenced by the substitution of Sr^{2+} ion by Nd^{3+} ion and Fe^{3+} ion by Zn^{2+} ion. The remanence (B_r), magnetic induction coercivity (H_{cb}), and intrinsic coercivity (H_{cj}) at the room temperature are derived from the demagnetizing curves of the hexaferrites samples with different Nd-Zn content (x).

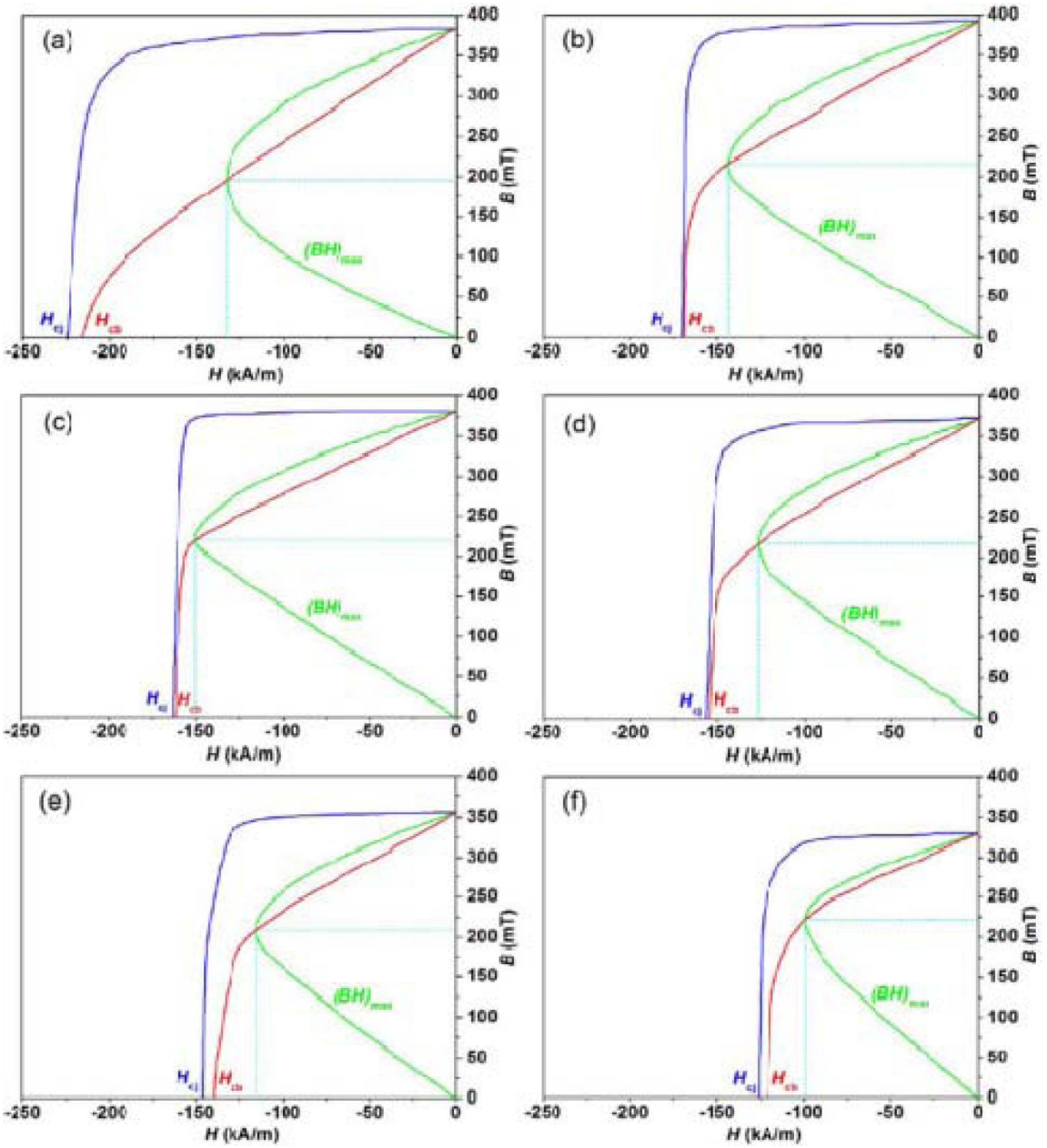

Fig. 3. Room temperature demagnetizing curves of the hexaferrites $Ba_{0.40}Sr_{0.60-x}Nd_xFe_{12.00-x}Zn_xO_{19}$ with (a) x = 0.00, (b) x = 0.06, (c) x = 0.12, (d) x = 0.18, (e) x = 0.24, and (f) x = 0.30.

The remanence (B_r) of the hexaferrites $Ba_{0.40}Sr_{0.60-x}Nd_xFe_{12.00-x}Zn_xO_{19}$ as a function of Nd-Zn content (x) is plotted in Fig. 4(a). It is clearer that a suitable amount of Nd-Zn substitution can increase the remanence (B_r) of the hexaferrites. In Fig. 4(a), with increasing Nd-Zn content (x), B_r first increases and reaches to the maximum value of 386.0 mT at Nd-Zn content (x) = 0.06, and then decreases when Nd-Zn content (x) $\geq$ 0.06. The changing trend of remanence (B_r) can be explained on the basis of the occupation of the substituted ions and the impurity phase. M-type hexaferrites belong to $P6_3/mmc$ space group, and have five crystallographic sublattices, such as three kinds of octahedral sites (2*a*, 12*k*, 4f_2), one tetrahedral site (4f_1) and one bipyramidal site (2*b*). The 2*a*, 12*k* and 2*b* sites have upward spin direction, and the 4f_1 and 4f_2 sites have downward spin direction [37, 40]. Herme et al. [41] have reported that in the M-type hexaferrites, Nd^{3+} ions substitute the Sr^{2+} sites in the vicinity of 4f_2 sites via Mössbauer analysis. Lee et al. [42] have reported that Zn^{2+} ions prefer to occupy the 4f_1 and 2*b* sites of tetrahedral sites in the M-type hexagonal structure by Mössbauer spectra. Zn^{2+} ion is nonmagnetic. And the magnetic moment of Fe^{3+} ion is 5 μ_B. Therefore, the increase of remanence (B_r) for the hexaferrites with increasing Nd-Zn content (x) from 0.00 to 0.06 is probably due to the below factor. When Nd-Zn content (x) $\leq$ 0.06, the number of Zn^{2+} ions entering 4f_1 sites (spin down) is more than that

of Zn^{2+} ions entering 2*b* sites (spin up). This in turn decreases the negative magnetic moment of Fe^{3+} ions. Consequently, according to equation (3), the whole magnetic moment is enhanced. This leads to the increase of the remanence (B_r). When Nd-Zn content (x) ≥ 0.06, the decrease of remanence (B_r) for the hexaferrites may be attributed to the below three reasons. Firstly, at Nd-Zn content (x) ≥ 0.06, Zn^{2+} ions substitute Fe^{3+} ions in 2*b* sites having spin-up. According to equation (3), this in turn decreases the whole magnetic moment. This results in the decrease of the remanence (B_r). Secondly, Zn^{2+} (0 μ_B) ions substituting magnetic Fe^{3+} ions (5 μ_B) weaken the super-exchange interaction between metallic ions in the M-type hexaferrites, and then the remanence (B_r) is decreased. Thirdly, when Nd-Zn content (x) = 0.30, as seen from Fig. 1, the impurity phase (hematite: α-Fe_2O_3) leads to the decrease of remanence (B_r).

Fig. 4(b) shows the intrinsic coercivity (H_{cj}) and magnetic induction coercivity (H_{cb}) of the hexaferrites $Ba_{0.40}Sr_{0.60-x}Nd_xFe_{12.00-x}Zn_xO_{19}$ as a function of Nd-Zn content (x). As shown in Fig. 4(b), the values of H_{cj} and H_{cb} show a decreasing trend with increasing Nd-Zn content (x), and decrease from 225.0 and 215.9 kA/m at x = 0.00 to 126.2 and 120.7 kA/m at x = 0.30, respectively. This proposes that Nd-Zn co-substitution

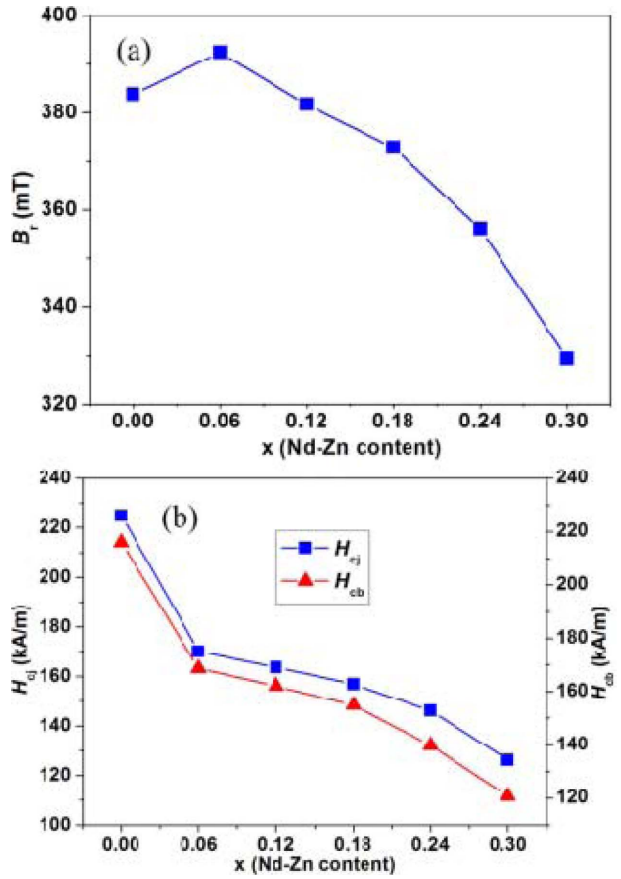

Fig. 4. (a) Remanence (B_r), and (b) Intrinsic coercivity (H_{cj}) and magnetic induction coercivity (H_{cb}) of the hexaferrites $Ba_{0.40}Sr_{0.60-x}Nd_xFe_{12.00-x}Zn_xO_{19}$ as a function of Nd-Zn content (x).

can modify the coercivity of M-type Ba-Sr hexaferrites. Yang et al. [43] have reported that in the M-type hexaferrites, the ions at octahedral 4f_2 site and bipyramidal 2*b* site are known to be the main contributors to the magnetocrystalline anisotropy. According to the Stroner-Wohlfarth theory, the intrinsic coercivity (H_{cj}) of the M-type hexaferrites which results from coherent rotation of magnetization can be calculated by the following equation [44]:

$$H_{cj} = C\left[\frac{2K_1}{M_s} - N \times M_s\right], \quad (4)$$

where C is dimensionless constant of material, K_1 is the first anisotropy constant, and N is the grain demagnetization factor. Therefore, according to the equation (4), the decrease of H_{cj} with increasing Nd-Zn content (x) from 0.00 to 0.30 could be due to the following two reasons. Firstly, as seen from Fig. 2, the average grain size of M-type hexaferrite increases with increasing Nd-Zn content (x) from 0.00 to 0.30. Thus, the value of N increases with increasing Nd-Zn content (x). According to equation (4), the value of H_{cj} is decreased. Secondly, the results of Mössbauer spectra showed that Zn^{2+} ions prefer to occupy the 4f_1 and 2*b* sites of tetrahedral sites in the M-type hexagonal structure [42]. The decrease of H_{cj} with increasing Nd-Zn content (x) may be related to the reduction of magnetocrystalline anisotropy field as a result of Zn^{2+} substitution for Fe^{3+} ions at 2b sites.

The temperature dependent demagnetizing curves of the hexaferrites $Ba_{0.40}Sr_{0.60-x}Nd_xFe_{12.00-x}Zn_xO_{19}$ with different Nd-Zn content (x) are presented in Fig. 5. The changing trend of the demagnetizing curves measured at different temperatures is in agreement with that reported by T.D.K. Corporation [45] and A. Goldman et al. [46]. The values of the remanence (B_r), and intrinsic coercivity (H_{cj}) at different temperatures are calculated from the demagnetizing curves for the hexaferrites with different Nd-Zn content (x). Fig. 6(a) presents the temperature dependent remanence (B_r) between 20 °C and 140 °C for the hexaferrites with different Nd-Zn content (x). As seen from Fig. 6(a), for the hexaferrites with different Nd-Zn content (x), the values of remanence (B_r) have a linear decreasing behavior with increasing temperature from 20 °C to 140 °C. This is in agreement with the results reported by Zhou et al. [47]. The variations of the intrinsic coercivity (H_{cj}) between 20 °C and 140 °C for the hexaferrites $Ba_{0.40}Sr_{0.60-x}Nd_xFe_{12.00-x}Zn_xO_{19}$ with different Nd-Zn content (x) are shown in Fig. 6(b). It is observed that for the hexaferrites with different Nd-Zn content (x), the values of intrinsic coercivity (H_{cj}) raise linearly with increasing temperature from 20 °C to 140 °C. This agrees with the changing trend reported by W. Zhou [48] and T.D.K. Corporation [49].

When the ambient temperature ≤ 400 °C, the remanence

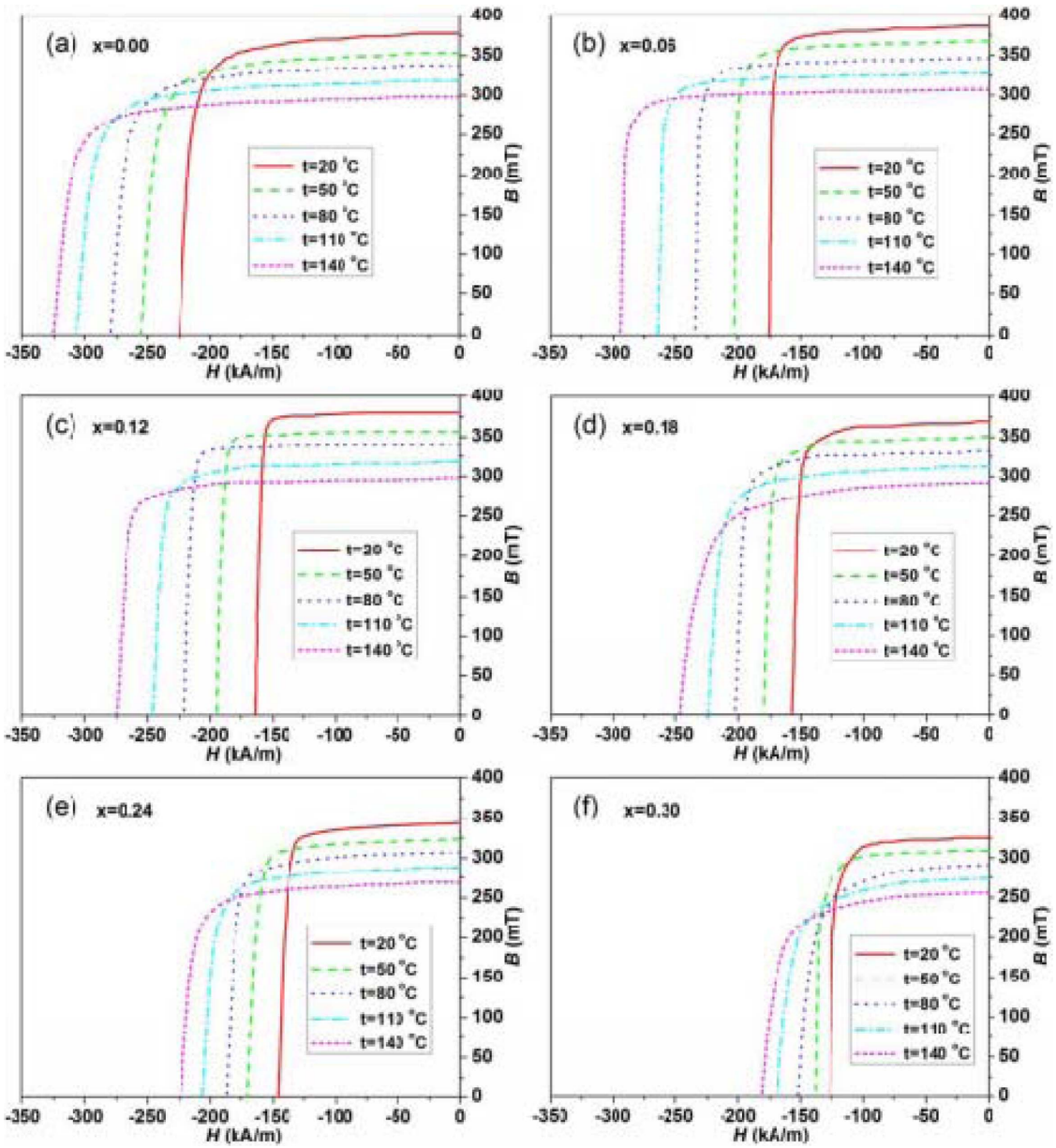

Fig. 5. Measuring temperature dependent demagnetizing curves of the hexaferrites $Ba_{0.40}Sr_{0.60-x}Nd_xFe_{12.00-x}Zn_xO_{19}$ with (a) x=0.00, (b) x=0.06, (c) x=0.12, (d) x=0.18, (e) x=0.24, and (f) x=0.30.

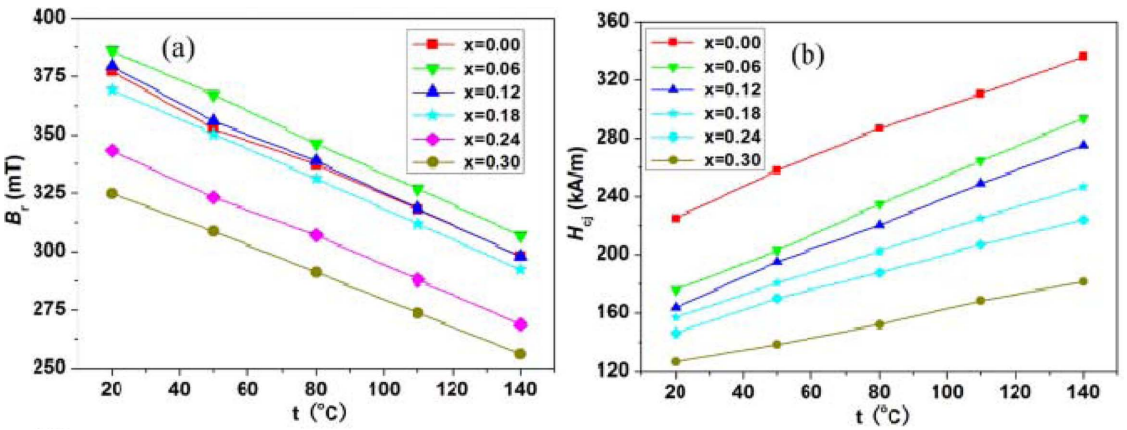

Fig. 6. (a) The temperature dependent remanence (B_r), and (b) The temperature dependent intrinsic coercivity (H_{cj}) of the hexaferrites $Ba_{0.40}Sr_{0.60-x}Nd_xFe_{12.00-x}Zn_xO_{19}$ with different Nd-Zn content (x) from x=0.00 to x=0.30, obtained from demagnetizing curves.

(B_r) of hexaferrites $BaFe_{12}O_{19}$ deareases linearly with increasing temperature [50]. The temperature coefficient of remanence (B_r) can be approximated as a constant in a certain temperature range. Therefore, the average temperature coefficient of B_r (a_{Br}) of hexaferrites can be defined as the below relation [48]:

$$\alpha_{Br} = \frac{B_r(t) - B_r(20)}{B_r(20)(t-20)} \times 100\% , \quad (5)$$

where $B_r(20)$ is the value of remanence (B_r) measured at 20 °C, $B_r(t)$ is the value of remanence (B_r) measured at temperature of t °C. Fig. 7(a) represents the variation of a_{Br} of the hexaferrites $Ba_{0.40}Sr_{0.60-x}Nd_xFe_{12.00-x}Zn_xO_{19}$ as a function of Nd-Zn content (x). It is clear from Fig. 7(a) that the value of a_{Br} basically remains constant around -0.175 %/°C. The value of a_{Br} is in agreement with that reported by T.D.K. Corporation [45]. This indicates that the Nd-Zn substitution have not big impact on the average temperature coefficient of remanence (B_r) (a_{Br}) of the hexaferrites $Ba_{0.40}Sr_{0.60-x}Nd_xFe_{12.00-x}Zn_xO_{19}$.

As shown in Fig. 6(b), the values of intrinsic coercivity (H_{cj}) have a linear behavior with temperature from 20 °C to 140 °C. The temperature coefficient of intrinsic coercivity (H_{cj}) is also approximated as a constant in a certain temperature range [49]. Thus, the average temperature coefficient of H_{cj} (a_{Hcj}) can be calculated using the following equation [43]:

$$\alpha_{Hcj} = \frac{H_{cj}(t) - H_{cj}(20)}{H_{cj}(20)(t-20)} \times 100\% , \quad (6)$$

where $H_{cj}(20)$ is the value of intrinsic coercivity (H_{cj}) measured at 20 °C, $H_{cj}(t)$ is the value of intrinsic coercivity (H_{cj}) measured at temperature of t °C. The influence of Nd-Zn content (x) on the average temperature coefficient of intrinsic coercivity (H_{cj}) (a_{Hcj}) of the hexaferrites $Ba_{0.40}Sr_{0.60-x}Nd_xFe_{12.00-x}Zn_xO_{19}$ is plotted in Fig. 7(b). It is noted that the value of a_{Hcj} firstly increases from 0.417 %/°C at x=0.00 to 0.573 %/°C at x = 0.12, and then decreases when Nd-Zn content (x) ≥ 0.12. This shows that Nd-Zn content (x) can significantly affect the values of a_{Hcj}. The values of a_{Hcj} are larger than that reported by T.D.K. Corporation [49], which should the values of intrinsic coercivity (H_{cj}) in this study are lower than that in TDK Products Catalog [49].

Fig. 8 illustrates the impact of Nd-Zn content (x) on the DC electrical resistivity (ρ) of the hexaferrites $Ba_{0.40}Sr_{0.60-x}Nd_xFe_{12.00-x}Zn_xO_{19}$. It is clear that the electrical resistivity (ρ) is strongly affected by Nd-Zn content (x). It is observed that the value of electrical resitivity (ρ) decreases from 679.9×10^7 Ω-Cm at x = 0.00 to 0.13×10^7 Ω-Cm at x = 0.30. The mechanism of conductivity in the hexaferrites is attributed to the hopping of electrons between Fe^{3+} and Fe^{2+} ions at the octahedral sites [50]. Van Diepen et al. have reported that the substitution of La^{3+} for Ba^{2+} or Sr^{2+} in M-type ferrites is associated with a valence change of Fe^{3+} to Fe^{2+} at 2*a* or $4f_2$ site [51]. Thus, as Nd^{3+} ions substitute Sr^{2+} ions and Zn^{2+} ions substitute Fe^{3+} ions, some Fe^{3+} ions will change into Fe^{2+} ions. This increases the number of Fe^{2+} ions which leads to the increase of the hopping

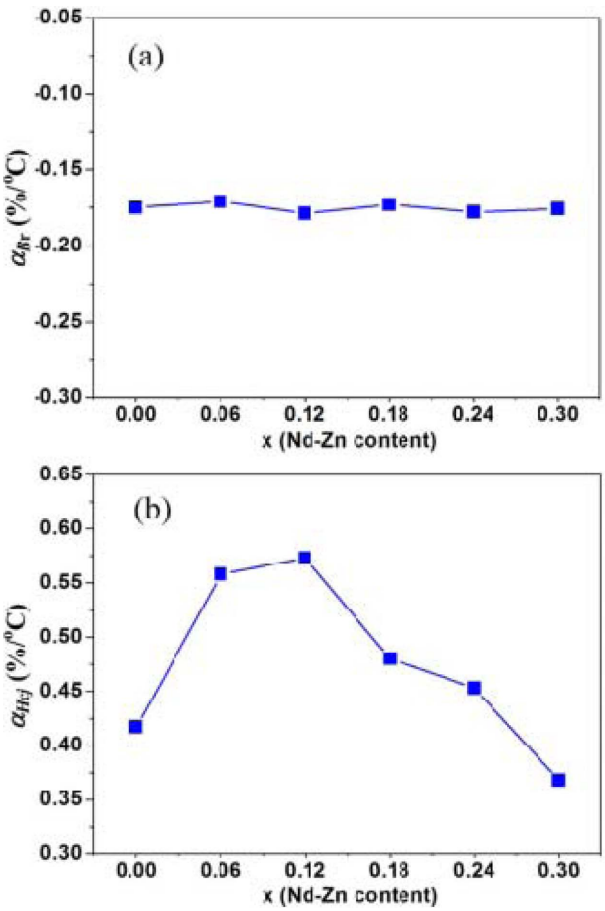

Fig. 7. (a) The average temperature coefficient of remanence (B_r) (a_{Br}), and (b) The average temperature coefficient of intrinsic coercivity (H_{cj}) (a_{Hcj}) of the hexaferrites $Ba_{0.40}Sr_{0.60-x}Nd_xFe_{12.00-x}Zn_xO_{19}$ as a function of Nd-Zn content (x).

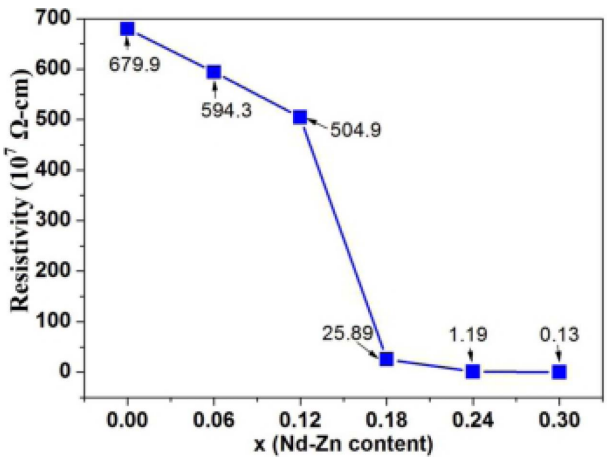

Fig. 8. DC electrical resistivity (ρ) of the hexaferrites $Ba_{0.40}Sr_{0.60-x}Nd_xFe_{12.00-x}Zn_xO_{19}$ as a function of Nd-Zn content (x).

probability between the Fe^{3+} and Fe^{2+} ions. Thus, the above reasons result in the decrease of electrical resitivity (ρ).

Conclusion

The solid-state reaction route was used to synthesize the Nd-Zn substituted M-type hexaferrites with nominal compositions $Ba_{0.40}Sr_{0.60-x}Nd_xFe_{12.00-x}Zn_xO_{19}$ ($0.00 \leq x \leq 0.30$). The X-ray diffraction patterns show that the hexaferrites with Nd-Zn content (x) of $0.00 \leq x \leq 0.24$ were single M-type phase, while the hexaferrites with Nd-Zn content (x) = 0.30 exhibited the M-type phase and impurity phases. FE-SEM images proposed that all the particles were regular hexagonal platelet-like shape and the average particle size increased with increasing Nd-Zn content (x). B_r increased with Nd-Zn content (x) from 0.00 to 0.06, and then started to decrease when Nd-Zn content (x) $\geq$ 0.06. H_{cj} and H_{cb} decreased with Nd-Zn content (x) from 0.00 to 0.30. B_r indicated a linear decreasing behavior with increasing temperature from 20 °C to 140 °C. H_{cj} raise linearly with increasing temperature from 20 °C to 140 °C. The value of a_{Br} basically remained constant with Nd-Zn content (x). The value of a_{Hcj} firstly increased with x from 0.00 to 0.12, and then decreased when $x \geq 0.12$. The electrical resitivity (ρ) presented a decreasing trend with x from 0.00 to 0.30.

Acknowledgements

This work was supported by the National Natural Science Foundation of China (Nos. 51872004, 51802002), Education Department of Anhui Province (Nos. KJ 2013B293, KJ2018A0039), Key Program of the Science and Technology of Anhui Province (Grant No. S2019 04a09020074).

References

1. S.V. Trukhanov, A.V. Trukhanov, V.A. Turchenko, An.V. Trukhanov, E.L. Trukhanova, D.I. Tishkevich, V.M. Ivanov, T.I. Zubar, M. Salem, V.G. Kostishyn, L.V. Panina, D.A. Vinnik, S.A. Gudkova, Ceram. Int. 44 (2018) 290-300.
2. L.A. Trusov, E.A. Gorbachev, V.A. Lebedev, A.E. Sleptsova, I.V. Roslyakov, E.S. Kozlyakova, A.V. Vasiliev, R.E. Dinnebier, M. Jansen, P.E. Kazin, Chem. Commun. 54 (2018) 479-482.
3. T.T. Loan, T.T.V. NGA, N.P. Duong, S. Soontarnon, T.D. Hien, J. Electron. Mater. 46 (2017) 3396-3405.
4. I. Ali, M.U. Islam, M.S. Awan, M. Ahmad, J. Electron. Mater. 43 (2014) 512-521.
5. R. Valenzuela, in "Magnetic ceramics" (Cambridge University Press, 1994) p.191.
6. D. Makovec, D. Primc, S. Šturm, A. Kodre, D. Hanžel, M. Drofenik, J. Solid State Chem. 196 (2012) 63-71.
7. S. Mahadevan, S.B. Narang, P. Sharma, Ceram. Int. 45 (2019) 9000-9006.
8. N. Tran, H.S. Kim, T.L. Phan, D.S. Yang, B.W. Lee, Ceram. Int. 44 (2018) 12132-12136.
9. J. Dho, E.K. Lee, J.Y. Park, N.H. Hur, J. Magn. Magn. Mater. 285 (2005) 164-168.
10. C. Serletis, G. Litsardakis, E. Pavidou, K.G. Efthimiaadis, Physica B. 525 (2017) 78-83.
11. Z.H. Hua, S.Z. Li, Z.D. Han, D.H. Wang, M. Lu, W. Zhong, B.X. Gu, Y.W. Du, Mater. Sci. Eng. A 448 (2007) 326-329.
12. J.E. Beevers, C.L. Love, V.K. Lazarov, S.A. Cavill, H. Izadkhah, C. Vittoria, R. Fan, G. van der Laan, S.S. Dhesi, App. Phys. Lett. 112 (2016) 082401.
13. X.X. Wei, Y.H. Liu, D.J. Zhao, X.W. Mao, W.Y. Jiang, S.Z. Sam Ge, J. Magn. Magn. Mater. 493 (2020) 165664.
14. J.F. Wang, C.B. Ponton, I.R. Harris, J. Alloys Compd. 403 (2005) 104-109.
15. A. Singh, S.B. Narang, K. Singh, O.P. Pandey, R.K. Kotnala, J. Ceram. Process. Res. 11[2] (2010) 241–249.
16. A. Thakur, R.R. Singh, P.B. Barman, J. Magn. Magn. Mater. 326 (2013) 35-40.
17. J.F. Wang, C.B. Ponton, I.R. Harris, IEEE Trans. Magn. 38 (2002) 2928-2930.
18. D. Shekhawat, A.K. Singh, P.K. Roy, J. Mol. Struct. 1179 (2019) 787-794.
19. Y.J. Yang, J.X. Shao, F.H. Wang, D.H. Huang, J. Ceram. Process. Res. 18[5] (2017) 394–398.
20. J.F. Wang, C.B. Ponton, I.R. Harris, J. Magn. Magn. Mater. 298 (2006) 122-131.
21. P.A. Pawar, S.S. Desai, Q.Y. Tamboli, S.E. Shirsath, S.M. Patange, J. Magn. Magn. Mater. 378 (2015) 59-63.
22. G. Litsardakis, I. Manolakis, C. Serletis, K.G. Efthimiadis, J. Magn. Magn. Mater. 316 (2007) 170-173.
23. D.A. Vinnik, A.S. Semisalova, L.S. Mashkovtseva, A.K. Yakushechkina, S. Nemrava, S.A. Gudkova, D.A. Zherebtsov, N.S. Perov, L.I. Isaenko, R. Niewa, Mater. Chem. Phys. 163 (2015) 416-420.
24. X.-S. Liu, L. Fetnandez-Garcia, F. Hu, D.-R. Zhu, M. Suárez, J.L. Menéndez, Mater. Chem. Phys. 133 (2012) 961-964.
25. M. Ghimire, S. Yoon, L. Wang, D. Neupane, J. Alam, S.R. Mishra, J. Magn. Magn. Mater. 454 (2018) 110-120.
26. D.A. Vinnik, A.Yu. Tarasova, D.A. Zherebtsov, L.S. Mashkovtseva, S.A. Gudkova, S. Nemrava, A.K. Yakushechkina, A.S. Semisalova, L.I. Isaenko, R. Niewa, Ceram. Int. 41 (2015) 9172-9176.
27. J. Qiu, Y. Wang, M. Gu, Mater. Lett. 60 (2006) 2728-2732.
28. I.A. Auwal, H. Güngüneş, A. Baykal, S. Güner, S.E. Shirsath, M. Sertkol, Ceram. Int. 42 (2016) 8627-8635.
29. A. Shayan, M. Abdellahi, F. Shahmohammadian, S. Jabbarzare, A. Khandan, H. Ghayour, J. Alloys Compd. 708 (2017) 538-546.
30. H.M. Khan, M.U. Islam, Y.B. Xu, M.N. Ashiq, I. Ali, M.A. Iqbal, M. Ishaque, Ceram. Int. 40 (2014) 6487-6493.
31. T.-Y. Hwang, J. Lee, H.-R. Lim, S.J. Jeong, G.-H. An, J. Kim, Y.-H. Choa, Ceram. Int. 43 (2017) 3879-3884.
32. L. Peng, L.Z. Li, X.X. Zhong, Y.B. Hu, S.M. Chen, J. Magn. Magn. Mater. 428 (2017) 73-77.
33. Z.Y. Zhang, X.X. Liu, X.J. Wang, Y.P. Wu, R. Li, J. Alloys Compd. 525 (2012) 114-119.
34. H.M. Khan, M.U. Islam, Y.B. Xu, M. Asif Iqbal, I. Ali, M. Ishaque, M.A. Khan, J. Sol-Gel. Sci. Technol. 75 (2015) 305-312.
35. Z. Lalegani, A. Nemati, J. Mater. Sci.: Mater. Electron. 26 (2015) 2134-2144.
36. C.C. Liu, X.C. Kan, F. Hu, X.S. Liu, S.J. Feng, J.Y. Hu, W. Wang, K.M. Ur Rehman, M. Shezad, C. Zhang, H.H. Li,

S.Q. Zhou, Q.Y. Wu, J. Alloy. Compd. 785 (2019) 452-459.
37. Y.J. Yang, D.H. Huang, J.X. Shao, F.H. Wang, Chin. J. Phys. 57 (2019) 250-260.
38. A. Majeed, M.A. Khan, F. ur Raheem, A. Hussain, F. Iqbal, G. Murtaza, M.N. Akhtar, I. Shakir, M.F. Warsi, J. Magn. Magn. Mater. 408 (2016) 147-154.
39. V.N. Dhage, M.L. Mane, M.K. Babrekar, C.M. Kale, K.M. Jadhav, J. Alloys Compd. 509 (2011) 4394-4398.
40. Y.J. Yang, X.S. Liu, D.L. Jin, Y.Q. Ma, Mater. Res. Bull. 59 (2014) 37-41.
41. C. Herme, S.E. Jacobo, P.G. Bercoff, B. Arcondo, Hyperfine Interact. 195 (2010) 205-212.
42. S.W. Lee, S.Y. An, In-Bo Shim, C.S. Kim, J. Magn. Magn. Mater. 290-291 (2005) 231-233.
43. Z. Yang, C.S. Wang, X.H. Li, H.X. Zeng, Mater. Sci. Eng. B 90 (2002) 142-145.
44. B.K. Rai, S.R. Mishra, V.V. Nguyen, J.P. Liu, J. Alloys Compd. 550 (2013) 198-203.
45. TDK Electronics, in "TDK Products Catalog: Ferrite Magnets" (TDK Electronics, 2011) p.3.
46. A. Goldman, in "Modern Ferrite Technology" (Springer, 2006) p.235.
47. Z.G. Zhou, in "Ferrite Magnetic Materials" (Science Press, 1981) p.646.
48. W.Y. Zhou, in "Design Technology of Permanent Magnet Ferrite and Magnetic Fluid" (University of Electronic Science and Technology Press, 1991) p.34.
49. TDK Electronics, in "TDK Products Catalog: Ferrite Magnets" (TDK Electronics, 2014) p.4.
50. F. Aen, M.F. Wasiq, M.U. Rana, H.M. Khan, H.A. Khan, Ceram. Int. 42 (2016) 16077-16083.
51. A.M. Van Diepen, F.K. Lotgering, J. Phys. Chem. Solids 35 (1974) 1641-1643.

Appendix

A nomenclature of symbols in this article

Nomenclature	
c	lattice parameter, in unit of Å
a	lattice parameter, in unit of Å
B_r	remanence, in unit of mT
H_{cb}	magnetic induction coercivity, in unit of kA/m
H_{cj}	intrinsic coercivity, in unit of kA/m
α_{Br}	average temperature coefficient of remanence (B_r), in unit of %/°C
α_{Hcj}	average temperature coefficient of intrinsic coercivity (H_{cj}), in unit of %/°C
ρ	electrical resistivity, in unit of Ω-Cm